

Article

Au-Decorated 1D SnO₂ Nanowire/2D WS₂ Nanosheet Composite for CO Gas Sensing at Room Temperature in Self-Heating Mode

Jae-Hun Kim , Isao Sakaguchi, Shunich Hishita , Taku T. Suzuki and Noriko Saito * 

National Institute for Materials Science, Tsukuba 305-0044, Japan; kim.jaehun@nims.go.jp (J.-H.K.); sakaguchi.isao@nims.go.jp (I.S.); hishita.shunichi@nims.go.jp (S.H.); suzuki.taku@nims.go.jp (T.T.S.)

* Correspondence: saito.noriko@nims.go.jp

Abstract: We have designed a new ternary structure to enhance the sensing properties of WS₂ nanosheet (NS)-based gas sensors at room temperature (RT) in self-heating mode. SnO₂ nanowires (NWs, 10–30 wt%) were added to WS₂ NSs and then Au nanoparticles (NPs) were deposited on the surface of the resulting composites by UV irradiation. The Au-decorated 10 wt% SnO₂–WS₂ composition showed the highest gas sensing properties. The presence of SnO₂ NWs on the WS₂ NSs effectively enhanced the diffusion and adsorption of gas species into deeper parts of the gas sensor. Furthermore, the chemical sensitization of Au (increase in oxygen ionosorption; spillover effect and catalytic effect towards CO) contributed to an enhanced response to CO gas. Gas sensing tests performed in the self-heating mode demonstrated the possibility of realizing a low-voltage, low-power-consumption CO gas sensor based on the Au-decorated 10 wt% SnO₂–WS₂. The sensor response under 60% relative humidity (RH) conditions was 84% of that under dry conditions, which shows that CO sensing is possible in wet environments at room temperature operation.



Citation: Kim, J.-H.; Sakaguchi, I.; Hishita, S.; Suzuki, T.T.; Saito, N. Au-Decorated 1D SnO₂ Nanowire/2D WS₂ Nanosheet Composite for CO Gas Sensing at Room Temperature in Self-Heating Mode. *Chemosensors* **2022**, *10*, 132. <https://doi.org/10.3390/chemosensors10040132>

Academic Editor: Dario Zappa

Received: 11 March 2022

Accepted: 28 March 2022

Published: 1 April 2022

Publisher's Note: MDPI stays neutral with regard to jurisdictional claims in published maps and institutional affiliations.



Copyright: © 2022 by the authors. Licensee MDPI, Basel, Switzerland. This article is an open access article distributed under the terms and conditions of the Creative Commons Attribution (CC BY) license (<https://creativecommons.org/licenses/by/4.0/>).

Keywords: gas sensor; WS₂ nanosheet; self-heating; SnO₂ nanowire; Au decoration

1. Introduction

Gas sensors are used for many different purposes, but their main applications are related to safety. One of the most poisonous gases, carbon monoxide (CO), is known as a silent killer [1]. CO causes hypoxia and cell death in human tissue because it can easily replace oxygen and combine with hemoglobin (Hb) in the blood to form carboxyhemoglobin (COHb), which reduces the oxygen-carrying ability of Hb [2]. CO is a colorless, tasteless, and odorless gas [3]; therefore, high-sensitivity detection of CO using gas sensors is necessary for safety.

Resistive gas sensors, which are made of semiconducting metal oxides such as SnO₂ [4] or two-dimensional (2D) transition metal dichalcogenides (TMDs) such as WS₂ [5], are among the most popular types of gas sensors due to their high sensitivity, high stability, fast dynamics, and low cost [6]. Two-dimensional material has very exciting optical and electrical properties from both theoretical and practical standpoints [7–11]. TMD-based gas sensors with a 2D structure can function at low or RT due to the high electron mobility and high surface area [12]. Among the TMDs, the monolayer WS₂ NS is a promising sensing material owing to its high thermal stability, high oxidative resistance, favorable band structure, and high phonon-limited electron mobility [13]. To enhance the sensor response, composite materials with heterojunctions and a 3D structure have been proposed [14,15].

For the detection of various gases by resistive gas sensors, high temperatures are often necessary to achieve the best performance. Sensor devices need heaters, but this hinders miniaturization and thus limits their practical application in portable and mobile devices. A good strategy for dealing with this problem is to operate the gas sensor in self-heating mode [16,17]. In this mode, a voltage is applied to the sensor and its temperature increases

by Joule heating [18]. The flow of the charge carriers generates heat inside the sensor material. The power of Joule heating, W , is calculated using the $W = V^2/R$ relationship, where V is the applied voltage and R is the resistance. W increases with an increase in the applied voltage. Therefore, sensing measurements can be performed at RT without heaters by applying an optimized voltage.

In this study, we investigated CO gas sensing at RT in self-heating mode using WS₂ NS-based composite gas sensors for low-voltage, low-power sensor devices. We used the p -type WS₂, which is sometimes produced depending on the process, but only a few sensor applications have been reported [19]. For the composites, SnO₂ NWs [20–23] were added to the WS₂ NSs to construct a 3D morphology, which provides an increased adsorption of gases into the depths of the composite gas sensor and enhances the sensor response. SnO₂ is a well-known n -type metal oxide and SnO₂ NWs are promising sensor materials because of their high sensitivity and 3D structure with high gas diffusivity [24,25]. Subsequently, Au NPs were deposited on the surface of the resultant 3D structure. Au NPs are known to act as a catalyst for oxygen dissociation and CO oxidation [26,27] and they have an effect on CO gas detection [28–30]. Gas sensing studies under self-heating conditions demonstrated the possibility of realizing a low-voltage, low-power-consumption CO gas sensor based on our proposed Au-decorated SnO₂ NW–WS₂ NS structure.

2. Experimental Procedure

2.1. Preparation of Pristine and Au-Decorated WS₂ NSs

In total, 5 mg of monolayer WS₂ NS powder (ACS Material, Pasadena, CA, USA) was first dispersed in 0.01 mL of 2-propanol for 15 min. A total of 0.075 μ L of the suspension was drop-coated (in three drops) onto prepared Si substrates. The substrates with deposited WS₂ were dried at 80 °C for 10 min. For Au NP decoration, 0.4 g of HAuCl₄·H₂O was initially dissolved in 2-propanol. The substrate with WS₂ NSs was then immersed into the Au solution, and Au NPs were coated onto the surfaces of the WS₂ NSs under UV irradiation for 15 s by a halogen lamp (0.11 mW/cm² and $\lambda = 360$ nm), followed by an annealing process at 500 °C for 30 min in the presence of N₂ gas. We have previously reported [28] that the size of the resultant Au NPs was 7.4 nm, and their density was 17 NPs per 50 nm². The heat-treated powders were subsequently scratched off from the Si substrate, dispersed in 2-propanol, and drop-coated onto a sensor substrate.

2.2. Preparation of SnO₂ NW/WS₂ NS Composites

SnO₂ NWs were grown by a vapor–liquid–solid (VLS) growth technique [31,32]. The Si substrate on which a 3 nm-thick Au catalyst layer was deposited was placed in a quartz tube furnace that contained a ceramic crucible with highly pure (99.9%) Sn powder (Sigma-Aldrich, St. Louis, MO, USA). SnO₂ NWs were grown at 900 °C for 5 min in the presence of N₂ (300 sccm) and O₂ (10 sccm) flowing gases. The as-grown SnO₂ NWs on the Si substrate were then scraped off and stored in a vial. The diameter and length of SnO₂ NWs were about 50 nm and 40 μ m.

As-synthesized SnO₂ NWs (10, 20, and 30 wt%) were dispersed in a 2-propanol suspension of WS₂ to form a WS₂-SnO₂ composite structure.

2.3. Preparation of Au NP-Coated SnO₂–WS₂ Composite Gas Sensors

After preparation of SnO₂–WS₂ composite gas sensors, Au NPs were coated on their surfaces as described in Section 2.1. Figure S1 schematically shows the procedure for preparation of the Au NP-decorated SnO₂–WS₂ composite gas sensors.

2.4. Characterization

The morphology of the products was investigated using scanning electron microscopy (SEM; JSM-6700F, JEOL, Tokyo, Japan) and transmission electron microscopy (TEM; JEM-2100F, JEOL). The chemical composition was determined using X-ray photoelectron spectroscopy (XPS; SigmaProbe, Thermo Fisher Scientific, Waltham, MA, USA) using an Al-

K α characteristic emission line ($E = 1486$ eV) with the C 1s peak used as a reference peak (284.8 eV). For self-heating studies, the applied voltage was changed in the range of 1–20 V. The temperature of the gas sensors in self-heating mode was measured at room temperature with an infrared thermometer (IT-480S, Horiba, Kyoto, Japan), and the distance was fixed at 30 mm. Ultraviolet photo-emission spectroscopy (UPS, PHI company-made VersaProbe, Kanahawa, Japan) was used to estimate the work function of *p*-type WS₂. He I (21.22 eV) was used as the emission light, and the pressure of the chamber used for the analysis was fixed at $\sim 2 \times 10^{-8}$ mbar.

2.5. Gas Sensing Studies

The sensor substrate used in this study was glass that was equipped with Au interdigitated electrodes (DRP-G-IDEAU5, Drop Sens, Asturias, Spain) with 5 μm pitch. The sensing materials were dispersed in 2-propanol (0.01 mL). Three drops of the solution were then released onto the substrate, which was then dried at 80 °C for 10 min. The sensing responses of the gas sensors to C₃H₆O, C₆H₆, C₆H₇, CH₄, and CO gases were measured. The gas concentration was set by adjusting the ratio of the target gas and dry air using mass flow controllers (total flow rate = 100 sccm). The gas chamber was located inside of a horizontal-type quartz furnace, connecting to the electrical measurement system (Keithley DMM6500, Cleveland, OH, USA) to record the current continuously. The sensor response was calculated as $R = R_a/R_g$ or R_g/R_a , where R_a and R_g are the resistance in the presence of air and the target gas, respectively. Different voltages were applied at RT for the self-heating operation mode. The response and recovery times were defined as the times required to attain a 90% change in the resistance upon the supply or removal of the target gas, respectively. To investigate the effect of humidity of the 10 wt% SnO₂–WS₂ composite in sensing test, we compared the sensing behaviors in dry and humid air.

3. Results and Discussion

3.1. Morphological and Chemical Studies

Figure 1 shows typical SEM images of the morphologies of pristine WS₂ and a 10 wt% SnO₂–WS₂ composite, respectively. We confirmed that SnO₂ NWs were dispersed among the WS₂ NSs (Figure 1b). This unique morphology is beneficial for sensing studies as it enlarges the active surface area between the SnO₂ NWs and WS₂ NSs for incoming gas molecules. Figure 2a–c show TEM images of the Au NP-decorated WS₂ NSs. The high-resolution TEM (HRTEM) image in Figure 2c clearly shows the lattice fringes related to the crystalline planes of Au and WS₂. The spacings between the parallel fringes were 0.236 and 0.27 nm, which are related to the (111) and (100) crystal planes of Au and WS₂, respectively [33,34]. Figure 2d–f show TEM images of the SnO₂–WS₂ composite in which Au NPs, SnO₂ NWs, and WS₂ NSs are clearly observable. The overall TEM analysis results indicated the successful formation of Au NPs, SnO₂ NWs, and WS₂ NSs in a unique structure.

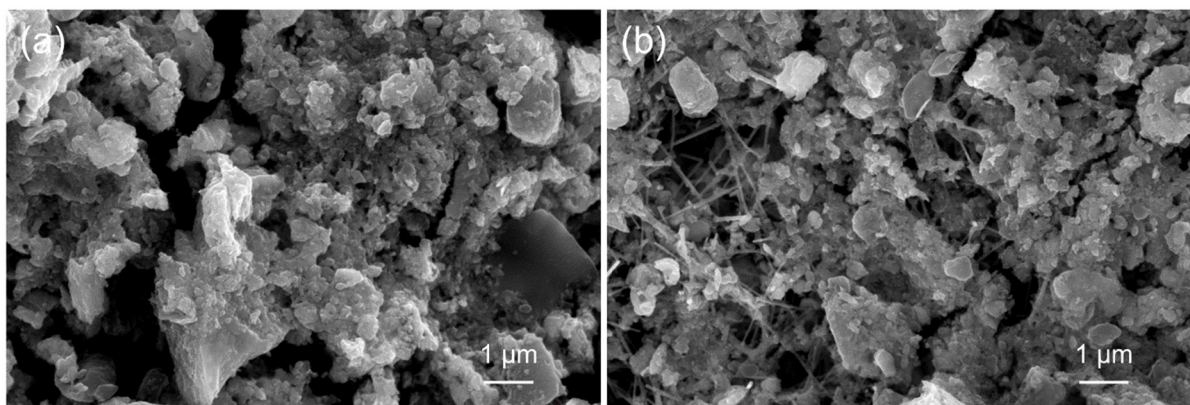


Figure 1. SEM images of (a) pristine WS₂ and (b) 10 wt% SnO₂–WS₂ composite.

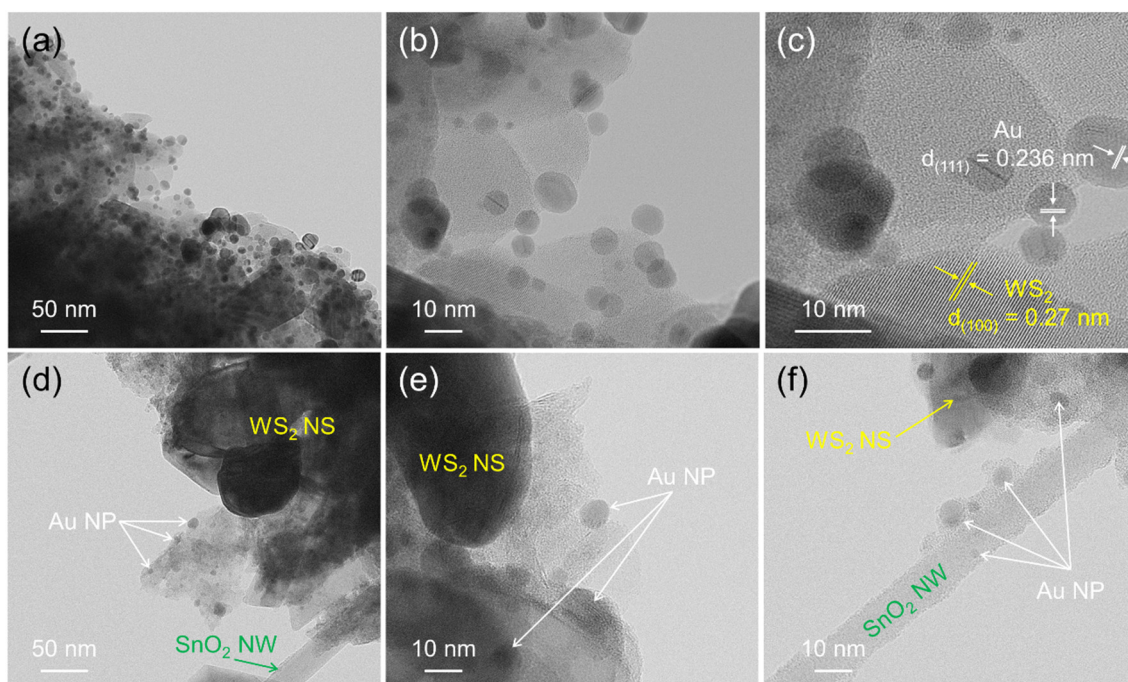


Figure 2. TEM analyses of (a–c) Au-decorated WS₂ NSs and (d–f) Au-decorated SnO₂–WS₂ composites.

Chemical analysis of the prepared sensor materials was performed using XPS. Based on the XPS results, all the expected elements were present in the synthesized sensing materials. An XPS survey of the Au-decorated SnO₂–WS₂ composite is shown in Figure S2a. The expected elements, i.e., W, S, Sn, O, and Au, are present. Figure S2b–f show the core-level regions of W 4f, S 2p, Sn 3d, O 1s, and Au 4f, respectively. Figure S2b shows that the W 4f peak is composed of W 5p_{3/2} (40.53 eV), W 4f_{7/2} (34.98 eV), and W 4f_{5/2} (37.23 eV) peaks. Two peaks can be observed in the S 2p region. The first peak, located at 161.53 eV, is related to S 2p and the second peak, located at 168.58 eV, is related to the S–O bond due to the partial adsorption of oxygen from the environment (Figure S2c). Figure S2d shows a high-resolution image of the Sn 3d region, which is composed of Sn 3d_{3/2} and Sn 3d_{5/2} peaks located at 494.88 and 486.63 eV, respectively. Additionally, a high-resolution image of the core-level region of O 1s is presented in Figure S2e. The Au 4f core-level region shown in Figure S2f is composed of two peaks, located at 83.28 and 86.98 eV, which can be attributed to Au 4f_{7/2} and Au 4f_{5/2}, respectively.

3.2. Gas Sensing Studies

3.2.1. Pristine and SnO₂–WS₂ NSs Gas Sensors without Au

We compared the sensor response to CO at RT under an applied voltage of 1 V, and the results are shown in Figure 3. The sensor behavior changed from the *p*-type to the *n*-type after adding 20 wt% or more of the *n*-type SnO₂ NWs to the *p*-type WS₂ NSs. The addition of SnO₂ NWs increased the baseline resistance of the gas sensors as SnO₂ has a higher resistance than WS₂. The sensor response was improved by the addition of SnO₂ NWs. The 30 wt% SnO₂–WS₂ composite and the SnO₂ sample did not show any sensor responses because of the low temperature conditions.

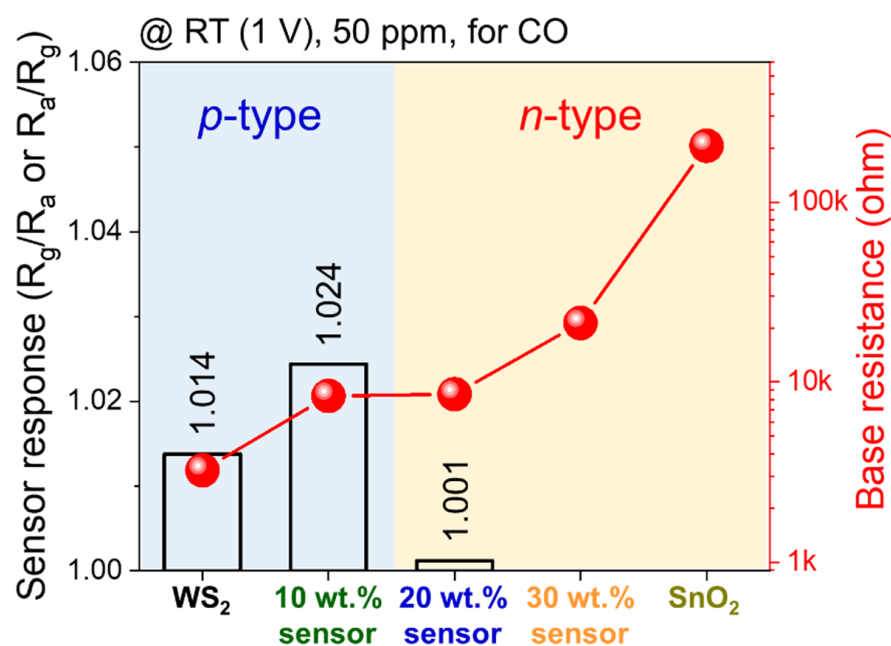


Figure 3. Comparison between the responses and base resistance of different gas sensors to 50 ppm CO at 20 °C under 1 V applied voltage.

The reproducibility test was conducted for pristine WS₂ gas sensors, which were annealed in N₂ atmosphere at 500 °C for 30 min using different sensor devices. As shown in Figure S3a, all of the devices showed a very small error value (0.001) in the sensor response. The baseline resistance of the sensor increased by more than a factor of two after annealing.

3.2.2. Au-Decorated Gas Sensors

We evaluated the effects of the Au NP decoration on the sensing properties for 50 ppm CO gas under an applied voltage of 1 V at RT (Figure 4). Figure 4e summarizes the responses of the gas sensors with and without Au NPs. Figure 4a–d show the normalized dynamic resistance plots. Au had a significant effect on the enhancement of the sensor response of WS₂ and the SnO₂–WS₂ composites. The 30 wt% SnO₂–WS₂ composite took a long time for recovery and did not show good results in repeated tests. For the pristine SnO₂ NWs, there was little effect of Au on the sensor response at this low temperature (Figure 4d). Figure 4f shows the baseline resistances in air and N₂ with Au NPs. The baseline resistance of the Au-decorated samples was higher than that of the samples without Au (Figure 3). The resistance in N₂, R_{N_2} , was larger than that in air, R_{air} , for the p-type WS₂ and 10 wt% SnO₂–WS₂ composite, and R_{N_2} was smaller than R_{air} for the n-type 30 wt% SnO₂–WS₂ composite and the SnO₂. For the 10 wt% SnO₂–WS₂ composite, the resistance ratios in N₂ and air, R_{N_2}/R_{air} , were 1.44 and 1.09 with and without Au, respectively. This reveals that the oxygen ionosorption was enhanced by the Au NPs. The 10 wt% SnO₂–WS₂ composite gas sensor showed the highest response; therefore, this sensor was selected for further studies.

Figure 5 indicates the selectivity patterns for the 10 wt% SnO₂–WS₂ gas sensor with and without Au for 50 ppm of various gases at RT and under an applied voltage of 1 V. In all cases, the response to the gases was increased after the Au decoration. In particular, the sensor response to CO was selectively improved due to the Au decoration. Overall, it can be concluded that Au decoration enhanced both the response and the selectivity of the gas sensors.

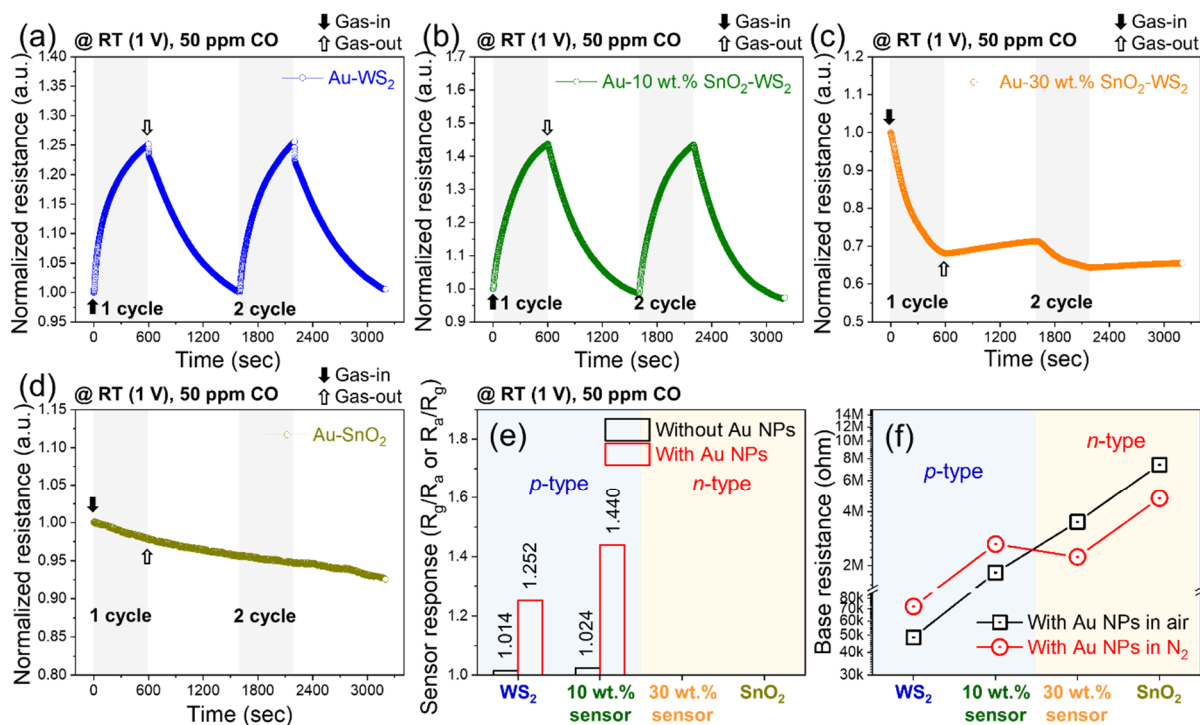


Figure 4. (a–d) Normalized dynamic resistance plots of different gas sensors to 50 ppm CO at room temperature (20 °C) under 1 V applied voltage. Comparison between the (e) sensor response and (f) base resistance of WS₂ NS, 10 wt% SnO₂-WS₂, 30 wt% SnO₂-WS₂, and SnO₂ NS gas sensors with Au NPs decoration in air and N₂ atmosphere.

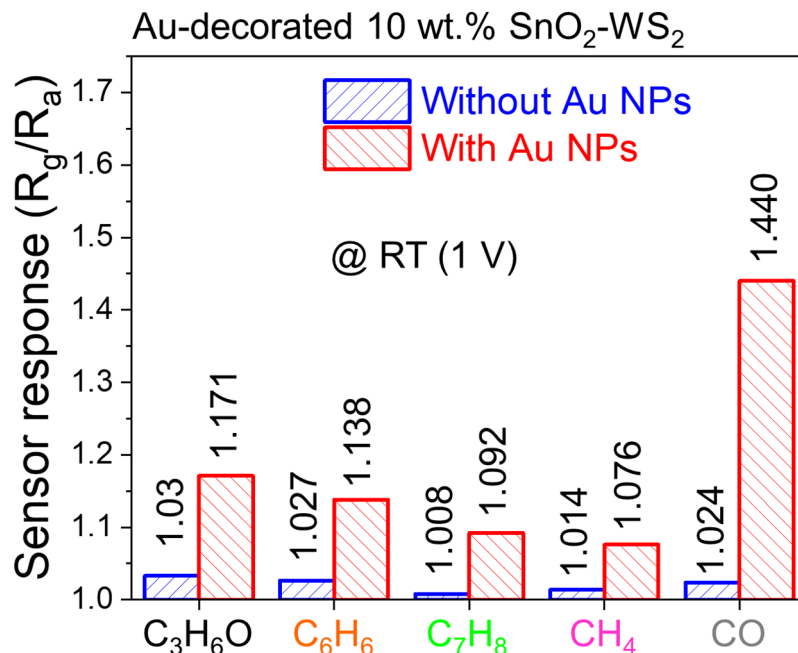


Figure 5. Selectivity pattern of Au-decorated 10 wt% SnO₂-WS₂ composite gas sensor without and with Au NPs measured under 1 V applied voltage at 20 °C.

3.2.3. Temperature Dependence

Figure 6a shows the hysteresis measurement results for the Au-decorated 10 wt% SnO₂-WS₂ composite gas sensor for 50 ppm CO gas under an applied voltage of 1 V, where the sensor temperature was increased from RT to 160 °C in the first step, and then was decreased to RT in the next step. Figure 6b compares the sensor response and baseline

3.2.4. Self-Heating Studies

In the next step, the self-heating effect on the gas sensor was evaluated for the Au-decorated 10 wt% SnO₂-WS₂ composite. The gas sensor response to ON/OFF for 50 ppm CO gas was measured at various applied voltages (1–20 V) at RT. CO gas was introduced at time 0 s (ON) and was stopped at time 600 s (OFF). The sensor responses are plotted in Figure 7a as a function of the applied voltage. The optimal applied voltage was found to be 6.8 V; therefore, further selectivity studies were performed at this voltage. Figure 7b shows the variations in the sensor baseline resistance and power consumption as a function of the applied voltage. The minimum baseline resistance was observed at an applied voltage of 15 V and the sensor electrode broke at 20 V. The power consumption was calculated using the $W = V^2/R$ relationship and it increased with an increase in the applied voltage. Under 6.8 V, the power consumption was about 95 μ W. Figure 7c shows the dynamic resistance curves of the sensor for 50 ppm of various gases, and the corresponding selectivity pattern is plotted in Figure 7d. The sensor showed a higher response to CO than to other gases, as in the case of 1 V (Figure 5).

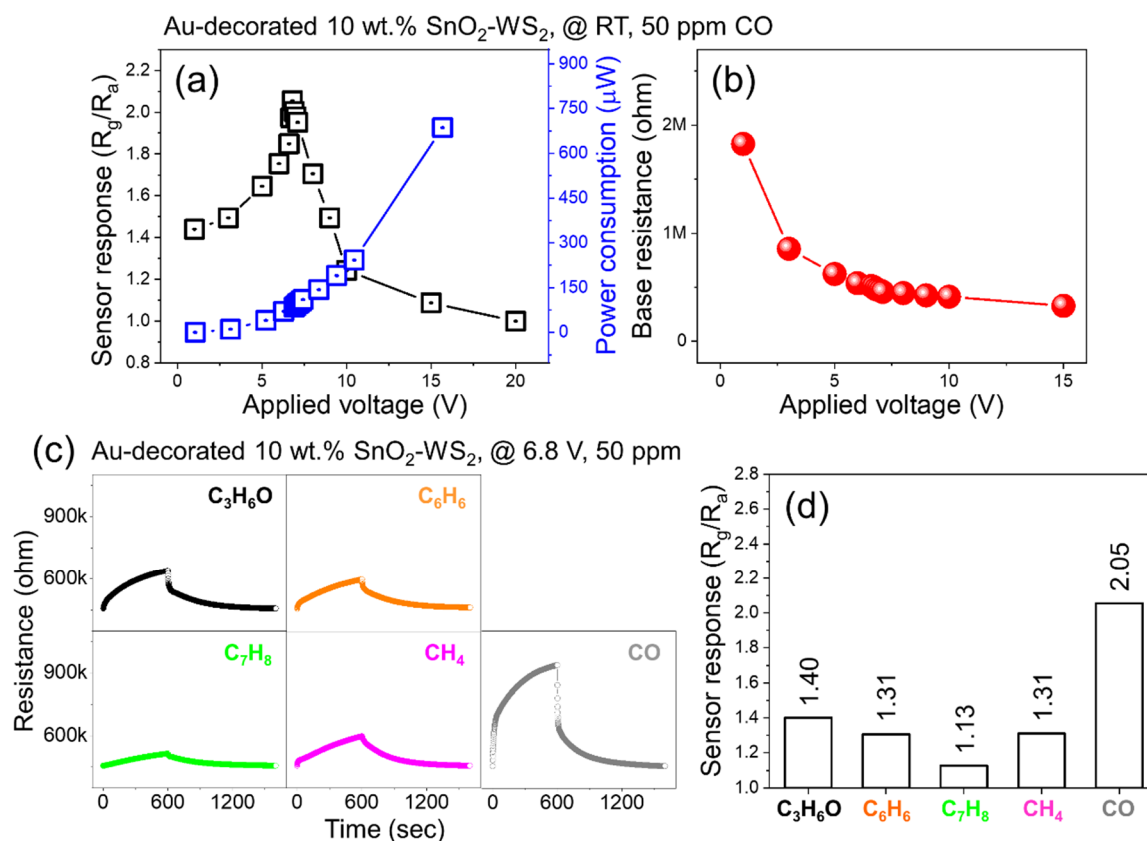


Figure 7. (a) Sensor response versus applied voltage for Au-decorated 10 wt% SnO₂-WS₂ gas sensor at 20 °C to 50 ppm CO gas. (b) Corresponding base resistance and power consumption versus applied voltage. (c) Dynamic resistance curves of 10 wt% SnO₂-WS₂ gas sensor to 50 ppm of different gases at 20 °C and under fixed 6.8 V applied voltage. (d) Corresponding selectivity pattern.

Figure S6 shows the dynamic resistance graphs for 50 ppm CO gas, the sensor response versus applied voltage, and the baseline resistance versus applied voltage measured at RT for the Au-decorated WS₂ (Figure S6a), Au-decorated SnO₂ (Figure S6d), and Au-decorated 30 wt% SnO₂-WS₂ (Figure S6g) gas sensors, for which the optimal applied voltage was 6.1, 17.3, and 13.1 V, respectively. The 10 and 30 wt% SnO₂-WS₂ composite gas sensors required a higher optimal voltage than the WS₂ gas sensor. This is due to the fact that the SnO₂ gas sensor requires a higher optimal voltage than the WS₂ gas sensor. The optimal applied voltage difference between the Au-decorated WS₂ and the Au-decorated 10 wt% SnO₂-WS₂

composite was 0.7 V. Despite this small difference, the Au-decorated SnO₂–WS₂ composite showed a higher sensor response (2.05) compared with that for the Au-decorated WS₂ gas sensor (1.59). The power consumption at the optimized voltage was 3 mW and 95 μ W for Au-decorated WS₂ and Au-decorated 10 wt% SnO₂–WS₂, respectively. Therefore, the present SnO₂–WS₂ composite is an effective sensor that can operate at a low voltage and low power consumption. For reference, the temperature change with respect to the applied voltage for each gas sensor without gas flow was measured using an infrared thermometer (Text S1 and Figure S7).

Figure 8 shows the performance of the Au-decorated 10 wt% SnO₂–WS₂ composite gas sensor under different RH conditions. Figure 8a shows the dynamic resistance plots of the Au-decorated 10 wt% SnO₂–WS₂ composite gas sensor for 50 ppm CO gas under 6.8 V external voltage at different RH conditions. The sensor response decreased with an increase in the RH (Figure 8b). The sensor response at 60% RH was 84% of that in dry air. The water vapor was adsorbed on the surface of the sensor, leading to a decrease in the available sites for the adsorption of oxygen in the air and a decrease in the CO effects. In Figure 8c, the response and recovery times under different RH conditions are plotted. While the effect of the RH on the response time was small, the recovery time became longer with an increase in the RH. The recovery process is the desorption of CO and the re-adsorption of oxygen, which is influenced by the water vapor. Reducing the impact of the water vapor for sensors operating at RT is our next challenge. Certain additives [35,36] and water absorbing filters [37,38] can minimize the influence of the RH.

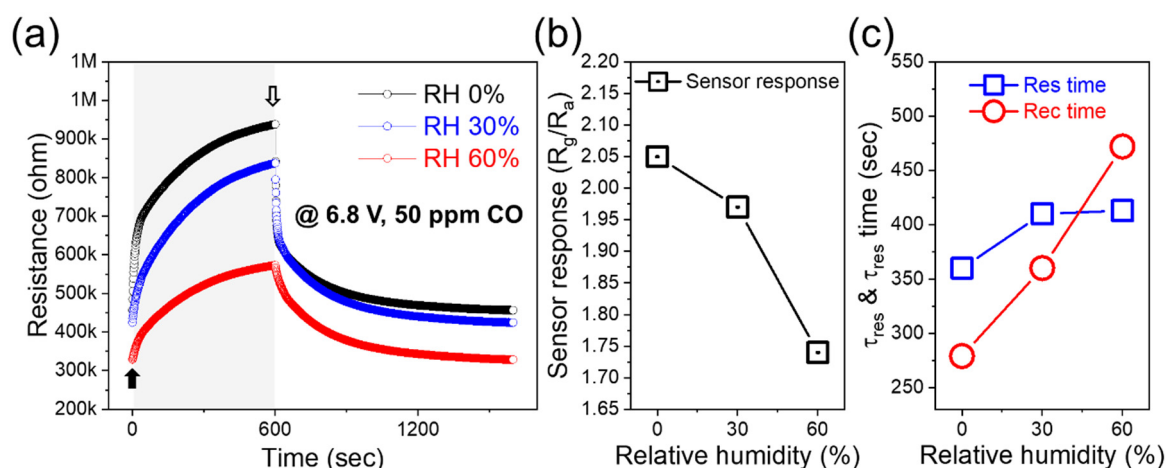


Figure 8. (a) Dynamic resistance curves of Au-decorated 10 wt% SnO₂–WS₂ gas sensor to 50 ppm CO gas under 6.8 V external voltage at different RH. Corresponding (b) sensor response, (c) response and recovery times as a function of RH.

In addition, Au-decorated 10 wt% SnO₂–WS₂ composite gas sensor showed excellent repeatability over ten cycles to 50 ppm of CO gas, at 6.8 V (Figure S8a,b). These results illustrate that the sensing properties of the gas sensor is maintained and that its robustness is supported by highly reproducible sensor responses. Additionally, long-term stability of the gas sensor was examined, with the results being represented in Figure S8c–e. The sensor shows excellent stability even after 3 months in the lab.

3.3. Gas Sensing Mechanism

The gas sensing mechanism of resistive gas sensors is based on variations of the resistance of the gas sensor in the presence of target gases [39,40]. For the pristine *p*-type WS₂ gas sensor, holes were the main carriers for the current [41]. In air, oxygen molecules are adsorbed on the surface of the gas sensor and they take electrons from the WS₂ due to the high electron affinity of oxygen molecules. Therefore, the concentration of holes increases relative to the conditions in N₂, resulting in the formation of a hole accumulation

layer (HAL). In the presence of a reducing gas such as CO, the reaction between the incoming CO molecules and the adsorbed oxygen ions causes the liberation of electrons at the sensor surface. The electrons combine with the holes, resulting in a thinner HAL and thus an increase in the resistance. Figure S9(b1) schematically show the sensing mechanism for a pristine *p*-type WS₂ gas sensor.

Figure S9(b2) show the sensing mechanism for *n*-type SnO₂ NW gas sensors. The main carriers are electrons. In air, oxygen molecules take electrons from the SnO₂ conduction band, which leads to the formation of an electron depletion layer (EDL) on SnO₂. In the presence of a reducing gas such as CO, the released electrons increase the concentration of electrons in the conduction band, so that the width of the EDL narrows to decrease the electrical resistance. The *p*-*n* junction between *p*-WS₂ and *n*-SnO₂ can cause the diffusion of carriers to maintain the equilibrium of the carrier concentrations (Figure S9c). As a depletion layer is created inside WS₂, the thickness of the HAL decreases (resistance increases). This is a disadvantage for *p*-type sensors for reducing gases.

In the present study, composites with SnO₂ showed a positive effect on the sensor response, which suggests that the effect of the *p*-*n* junction was small and the steric effect of the SnO₂ NWs was dominant for improving the sensor response. The SnO₂ NWs acted as a type of structure modifier so that the adsorption of gas species was improved by increasing the active surface area of the WS₂ NSs. When the WS₂ NSs were coated on the sensor substrate using the drop casting method, they formed a fairly dense structure due to the 2D nature of the WS₂ NSs, and the dense structure reduced the adsorption sites of the gaseous species. As shown in Figure S9a, by placing the 1D SnO₂ NWs between the 2D WS₂ NSs, a complex 3D structure was constructed inside the composite gas sensor. This architecture effectively improved the diffusion and adsorption of the gas species into deeper parts of the gas sensor by the steric effect of the SnO₂ NWs [42,43].

Next, we considered the electronic sensitization effects of Au on the *p*-type WS₂. Figure S10a shows that the ohmic contact between the *p*-type semiconductor (WS₂) and metal electrodes (Au) causes the electrons to move from the WS₂ to Au to equalize the Fermi levels if the work function of Au is larger than that of WS₂. Accordingly, as additional holes are created inside the WS₂, the HAL thickness expands and the sensor response can be improved. Conversely, (Figure S10b) a Schottky contact causes the electrons to move from Au to WS₂ if the work function of Au is smaller than that of WS₂. Accordingly, as a hole depletion layer (HDL) is created inside WS₂, the HAL thickness decreases (resistance increases), which is a disadvantage for *p*-type sensors.

In order to know the work functions, we took UPS measurements of the present *p*-type WS₂ NSs (Figure 9a). The high kinetic energy cutoff (E_{Fermi}), referred to as E_1 , and the low kinetic energy cutoff (E_{Cutoff}), referred to as E_2 , were used to find the W_f value (Figure 9b). The W_f value for the WS₂ NSs was determined to be 5.67 eV (i.e., $21.22 - 15.55 = 5.67$ eV) when we assumed that the electric potential was the same as the sample holder [44]. As this work function of WS₂ ($W_{f,WS_2} = 5.67$ eV) is larger than that of Au ($W_{f,Au} \approx 5.1$ eV [45]), the electrons will be transferred from Au to WS₂ to equalize the Fermi levels and as a result, a Schottky junction will be formed (Figure 9c) for the Au-decorated WS₂ NS sensor. The presence of the Au NPs forms the HDL of the WS₂ NSs, which increases the resistance and has the opposite effect of improving the sensor response. Therefore, we can conclude that the effect of Au on improving the sensing properties is due to chemical, not electronic, sensitization effects.

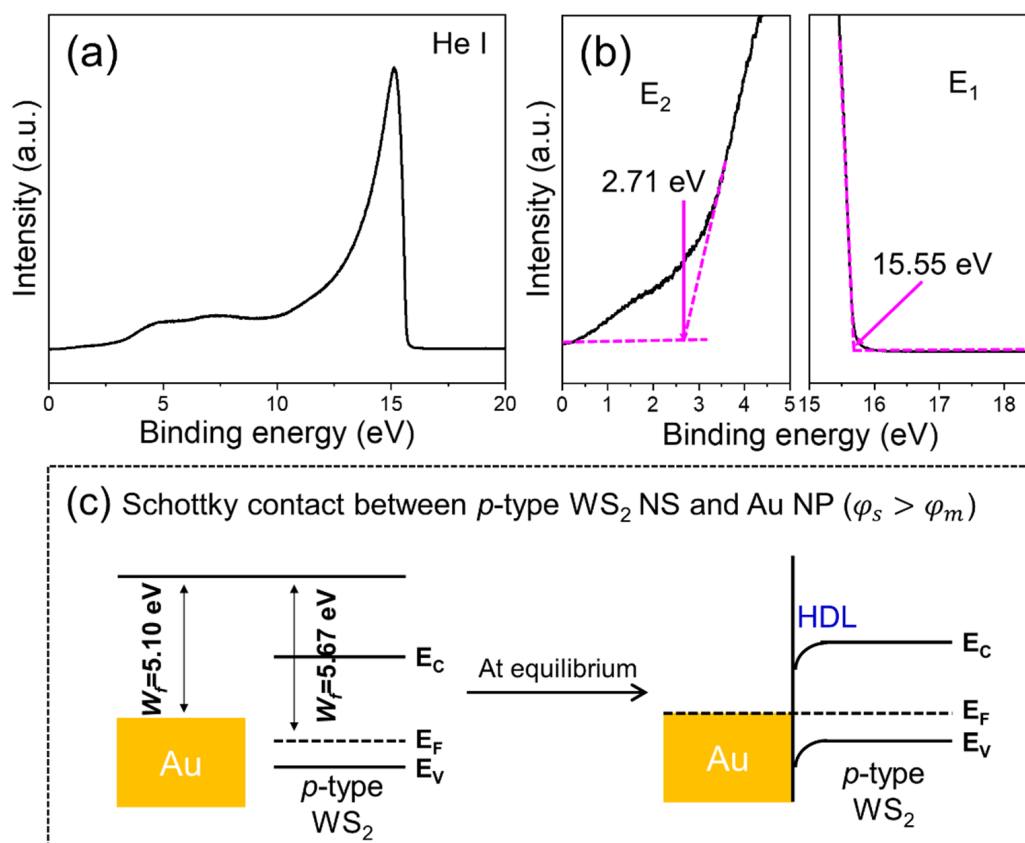


Figure 9. (a) UPS spectra of WS₂ NSs. (b) Corresponding energy cut off values of WS₂ NSs. (c) Band structures of WS₂ NSs and Au NPs before and after intimate contact.

Figure 10 shows the chemical sensitization effects of the Au NPs, the spillover effect [46] and catalytic effect. In the first mechanism, incoming oxygen gas molecules are adsorbed on the surface of Au and then become dissociated into ionic species. The species move to the surrounding medium and increase the ionosorption of oxygen on the surface of the gas sensor, resulting in more reactions between the oxygen and CO gas molecules. The higher resistance ratios in N₂ and air, R_{N_2}/R_{air} , of the Au-decorated samples suggest that the oxygen ionosorption was enhanced by the spillover effect of the Au NPs. In the second mechanism, Au works as the catalyst to lower the activation energy for CO oxidation. This effect resulted in improved sensor response and gas selectivity for CO. Table S1 lists the RT CO sensing properties of the present sensor with some 2D nanostructure-based gas sensors reported elsewhere. Overall, the present sensor showed a superior response to CO gas at RT, demonstrating its practical applications.

Figure S11 illustrates the Joule-heating effect of the Au-decorated 10 wt% SnO₂-WS₂ composite under an optimized voltage of 6.8 V. Under this voltage, WS₂ with low resistance generated enough heat to show the same level of sensor response at 160 °C. SnO₂ was only able to generate temperatures lower than 160 °C under this voltage. For the 10 wt% SnO₂-WS₂ composite, despite the fact that SnO₂ was warmed by the surrounding WS₂, the sensor response of the composite was the *p*-type and was larger than that without SnO₂. This suggests that the *n*-type SnO₂ has no effect due to its high resistance, which is about 24 times higher than that of WS₂ at 160 °C in air.

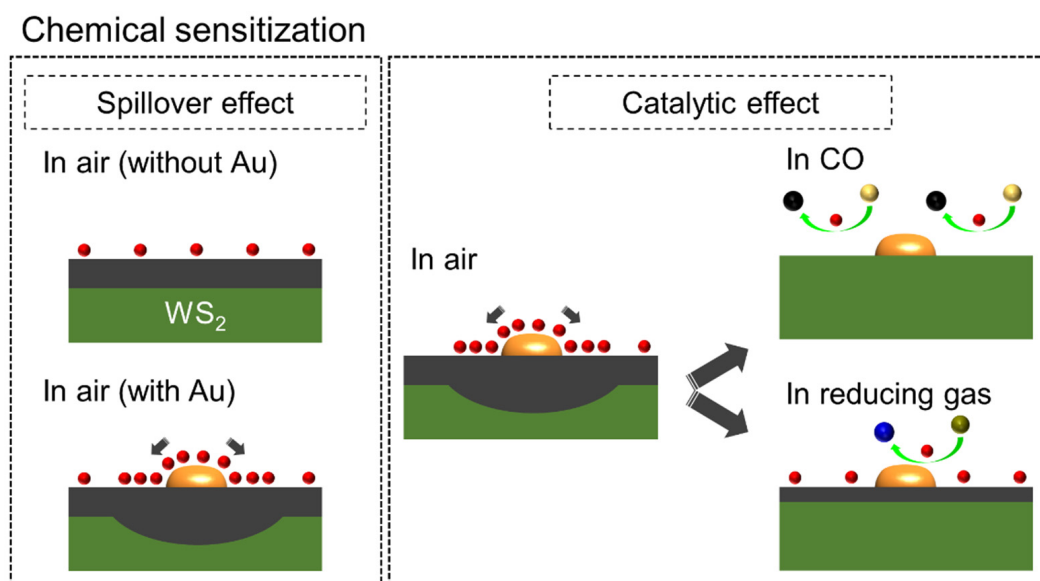


Figure 10. Gas sensing mechanism in chemical sensitization effects due to decorate the Au NPs.

4. Conclusions

A new sensor structure for CO detection at RT was designed using Au-decorated *n*-type SnO₂/*p*-type WS₂ composites. SnO₂ NWs grown using a VLS method were added (10, 20, and 30 wt%) to WS₂ NSs. The SnO₂ NWs were dispersed among the WS₂ NSs to construct a porous 3D morphology for CO sensing. The sensor behavior changed from the *p*-type to the *n*-type when 20 wt% or more of the *n*-type SnO₂ NWs was added to the *p*-type WS₂ NSs. The Au-decorated 10 wt% SnO₂–WS₂ composite gas sensor showed a *p*-type behavior and the highest sensitivity to CO gas. The SnO₂ NWs acted as a type of structure modifier so that the adsorption of gas species was improved by increasing the active surface area of the WS₂ NSs. The UPS analysis for the work function of the *p*-type WS₂ revealed that the chemical sensitization of Au NPs led to an enhanced sensor response in the ternary composite. Gas sensing in the self-heating mode using Joule heating for the materials demonstrated the possibility of a low-voltage, low-power-consumption CO gas sensor of the Au-decorated 10 wt% SnO₂–WS₂. The sensor response under 60% relative humidity conditions was 84% of that under dry conditions, which shows that CO sensing is possible in wet environments at RT operation. Further studies should be directed towards better microstructural control by improving the powder dispersion to make additional homogeneous sensing layers, reducing the humidity influence, and extending this approach to other similar systems such as SnS₂ and MoS₂.

Supplementary Materials: The following supporting information can be downloaded at: <https://www.mdpi.com/article/10.3390/chemosensors10040132/s1>, Table S1: A summary of CO gas sensing materials based on 2D nanostructures at low temperature. Figure S1: Schematic illustration of preparation of Au-decorated SnO₂–WS₂ gas sensors. Figure S2: XPS survey and core-level regions of Au-decorated 10wt% SnO₂–WS₂ composite. Figure S3: (a) Dynamic resistance curves of the pristine WS₂ gas sensors annealed in N₂ atmosphere at 500 °C for 30 min, where the sensor responses were obtained from three different sensor devices at 50 ppm of CO gas. (b) Corresponding base resistance. Figure S4: (a) Dynamic resistance curves of pristine WS₂ NS gas sensor to 50 ppm C₃H₆O gas at different temperatures (20–350 °C). (b) Corresponding response and base resistance versus temperature. Figure S5: (a–d) Normalized dynamic resistance plots of different gas sensors to 50 ppm CO at 160 °C under 1 V applied voltage. Comparison between the (e) sensor response and (f) base resistance of WS₂ NS, 10 wt% SnO₂–WS₂, 30 wt% SnO₂–WS₂, and SnO₂ NS gas sensors with Au NPs decoration in air and N₂ atmosphere. Figure S6: (a,d,g) Normalized dynamic resistance plots to 50 ppm CO at 20 °C under 1 V applied voltage. (b,e,h) Sensor responses and base resistance and (c,f,i) power consumption under different applied voltages at 20 °C for Au-decorated WS₂ NS, Au-

decorated SnO₂ NW, and Au-decorated 30 wt% SnO₂–WS₂ composite gas sensors. Figure S7: Sensor temperature versus applied voltage for different gas sensors. Text S1: Supplementary explanation for Figure S7. Figure S8: (a) Repeatability (ten sequential cycles) of Au-decorated 10 wt% SnO₂–WS₂ composite gas sensor to 50 ppm CO at 6.8 V. (b) Sensor response at different cycles. (c) Dynamic resistance curves to 50 ppm of CO for fresh sensor and those kept for 3 months at the laboratory. (d) Corresponding sensing response and (e) response times and recovery times. Figure S9: (a) Microscopic geometry of pristine WS₂ and SnO₂–WS₂ composite gas sensors on the surface of substrate. (b) Gas sensing mechanism in p-type WS₂ and n-type SnO₂ gas sensors. Energy-band diagrams showing (c) p-n junction. Figure S10: Energy-band diagrams showing (a) Ohmic contact with p-type semiconductor ($\phi_m > \phi_s$) and (b) Schottky contact with p-type semiconductor ($\phi_s > \phi_m$). Figure S11: Schematic of self-heating effects in Au-decorated 10 wt% SnO₂–WS₂ composite gas sensor. References [47–51] are cited in the supplementary materials.

Author Contributions: Conceptualization, formal analysis, investigation, data curation, writing—original draft preparation, and writing—review and editing, J.-H.K.; writing—review and editing, I.S., S.H. and T.T.S.; conceptualization, writing—original draft preparation, writing—review and editing, supervision, N.S. All authors have read and agreed to the published version of the manuscript.

Funding: This work was supported by JSPS KAKENHI Grant Nos. 17K06807 and 20F20343.

Institutional Review Board Statement: Not applicable.

Informed Consent Statement: Not applicable.

Data Availability Statement: Not applicable.

Acknowledgments: This work was supported by JSPS KAKENHI Grant Nos. 17K06807 and 20F20343. The authors also acknowledge the helpful discussion with K. Shimano. The author J.-H.K. thanks international research fellowship of the Japan society for the promotion of science.

Conflicts of Interest: The authors declare no conflict of interest.

References

1. Kulhari, L.; Ray, K.; Suri, N.; Khanna, P.K. Detection and characterization of CO gas using LTCC micro-hotplates. *Sādhanā* **2020**, *45*, 71. [[CrossRef](#)]
2. Prockop, L.D.; Chichkova, R.I. Carbon monoxide intoxication: An updated review. *J. Neurol. Sci.* **2007**, *262*, 122–130. [[CrossRef](#)] [[PubMed](#)]
3. Mirzaei, A.; Park, S.; Sun, G.-J.; Kheel, H.; Lee, C. CO gas sensing properties of In₄Sn₃O₁₂ and TeO₂ composite nanoparticle sensors. *J. Hazard. Mater.* **2016**, *305*, 130–138. [[CrossRef](#)] [[PubMed](#)]
4. Gupta, P.; Rathore, V. A comprehensive review: SnO₂ for photovoltaic and gas sensor applications. *Appl. Innov. Res.* **2019**, *1*, 184–193.
5. Donarelli, M.; Ottaviano, L. 2D materials for gas sensing applications: A review on graphene oxide, MoS₂, WS₂ and phosphorene. *Sensors* **2018**, *18*, 3638. [[CrossRef](#)]
6. Majhi, S.M.; Mirzaei, A.; Kim, H.W.; Kim, S.S.; Kim, T.W. Recent advances in energy-saving chemiresistive gas sensors: A review. *Nano Energy* **2020**, *79*, 105369. [[CrossRef](#)] [[PubMed](#)]
7. Zhang, Z.; Cai, R.; Long, F.; Wang, J. Development and application of tetrabromobisphenol A imprinted electrochemical sensor based on graphene/carbon nanotubes three-dimensional nanocomposites modified carbon electrode. *Talanta* **2015**, *134*, 435–442. [[CrossRef](#)]
8. Cheng, Z.; Liao, J.; He, B.; Zhang, F.; Zhang, F.; Huang, X.; Zhou, L. One-step fabrication of graphene oxide enhanced magnetic composite gel for highly efficient dye adsorption and catalysis. *ACS Sustain. Chem. Eng.* **2015**, *3*, 1677–1685. [[CrossRef](#)]
9. Xiao, L.; Youji, L.; Feitai, C.; Peng, X.; Ming, L. Facile synthesis of mesoporous titanium dioxide doped by Ag-coated graphene with enhanced visible-light photocatalytic performance for methylene blue degradation. *RSC Adv.* **2017**, *7*, 25314–25324. [[CrossRef](#)]
10. Tang, N.; Li, Y.; Chen, F.; Han, Z. In situ fabrication of a direct Z-scheme photocatalyst by immobilizing CdS quantum dots in the channels of graphene-hybridized and supported mesoporous titanium nanocrystals for high photocatalytic performance under visible light. *RSC Adv.* **2018**, *8*, 42233–42245. [[CrossRef](#)]
11. Chen, H.; Chen, Z.; Yang, H.; Wen, L.; Yi, Z.; Zhou, Z.; Dai, B.; Zhang, J.; Wu, X.; Wu, P. Multi-mode surface plasmon resonance absorber based on dart-type single-layer graphene. *RSC Adv.* **2022**, *12*, 7821–7829. [[CrossRef](#)]
12. Liu, D.; Tang, Z.; Zhang, Z. Comparative study on NO₂ and H₂S sensing mechanisms of gas sensors based on WS₂ nanosheets. *Sens. Actuators B* **2020**, *303*, 127114. [[CrossRef](#)]
13. Zhou, J.; Ma, C.; Kang, X.; Zhang, L.; Liu, X.-L. Effect of WS₂ particle size on mechanical properties and tribological behaviors of Cu-WS₂ composites sintered by SPS. *Trans. Nonferrous Met. Soc. China* **2018**, *28*, 1176–1185. [[CrossRef](#)]

14. Moon, W.J.; Yu, J.H.; Choi, G.M. The CO and H₂ gas selectivity of CuO-doped SnO₂-ZnO composite gas sensor. *Sens. Actuators B* **2002**, *87*, 464–470. [[CrossRef](#)]
15. Bang, J.H.; Choi, M.S.; Mirzaei, A.; Kwon, Y.J.; Kim, S.S.; Kim, T.W.; Kim, H.W. Selective NO₂ sensor based on Bi₂O₃ branched SnO₂ nanowires. *Sens. Actuators B* **2018**, *274*, 356–369. [[CrossRef](#)]
16. Tan, H.M.; Hung, C.M.; Ngoc, T.M.; Nguyen, H.; Hoa, N.D.; Duy, N.V.; Hieu, N.V. Novel self-heated gas sensors using on-chip networked nanowires with ultralow power consumption. *ACS Appl. Mater. Interfaces* **2017**, *9*, 6153–6162. [[CrossRef](#)]
17. Ngoc, T.M.; Duy, N.V.; Hoa, N.D.; Hung, C.M.; Nguyen, H.; Hieu, N.V. Effective design and fabrication of low-power-consumption self-heated SnO₂ nanowire sensors for reducing gases. *Sens. Actuators B* **2019**, *295*, 144–152. [[CrossRef](#)]
18. Kim, J.-H.; Mirzaei, A.; Bang, J.H.; Kim, H.W.; Kim, S.S. Selective H₂S sensing without external heat by a synergy effect in self-heated CuO-functionalized SnO₂-ZnO core-shell nanowires. *Sens. Actuators B* **2019**, *300*, 126981. [[CrossRef](#)]
19. Guang, Q.; Huang, B.; Li, X. Au-decorated WS₂ microflakes based sensors for selective ammonia detection at room temperature. *Chemosensors* **2022**, *10*, 9. [[CrossRef](#)]
20. Dattoli, E.N.; Wan, Q.; Guo, W.; Chen, Y.; Pan, X.; Lu, W. Fully transparent thin-film transistor devices based on SnO₂ nanowires. *Nano Lett.* **2007**, *7*, 2463–2469. [[CrossRef](#)]
21. Gubbala, S.; Chakrapani, V.; Kumar, V.; Sunkara, M.K. Band-edge engineered hybrid structures for dye-sensitized solar cells based on SnO₂ nanowires. *Adv. Funct. Mater.* **2008**, *18*, 2411–2418. [[CrossRef](#)]
22. Luo, L.; Liang, F.; Jie, J. Sn-catalyzed synthesis of SnO₂ nanowires and their optoelectronic characteristics. *Nanotechnology* **2011**, *22*, 485701. [[CrossRef](#)] [[PubMed](#)]
23. El-Maghraby, E.M.; Qurashi, A.; Yamazaki, T. Synthesis of SnO₂ nanowires their structural and H₂ gas sensing properties. *Ceram. Int.* **2013**, *39*, 8475–8480. [[CrossRef](#)]
24. Das, S.; Jayaraman, V. SnO₂: A comprehensive review on structures and gas sensors. *Prog. Mater. Sci.* **2014**, *66*, 112–255. [[CrossRef](#)]
25. Yamazoe, N.; Sakai, G.; Shimano, K. Oxide semiconductor gas sensors. *Catal. Surv. Asia* **2003**, *7*, 63–75. [[CrossRef](#)]
26. Kim, J.-H.; Wu, P.; Kim, H.W.; Kim, S.S. Highly selective sensing of CO, C₆H₆, and C₇H₈ gases by catalytic functionalization with metal nanoparticles. *ACS Appl. Mater. Interfaces* **2016**, *8*, 7173–7183. [[CrossRef](#)]
27. Kim, J.-H.; Mirzaei, A.; Kim, H.W.; Kim, S.S. Low power-consumption CO gas sensors based on Au-functionalized SnO₂-ZnO core-shell nanowires. *Sens. Actuators B* **2018**, *267*, 597–607. [[CrossRef](#)]
28. Kim, J.-H.; Mirzaei, A.; Kim, H.W.; Kim, S.S. Flexible and low power CO gas sensor with Au-functionalized 2D WS₂ nanoflakes. *Sens. Actuators B* **2020**, *313*, 128040. [[CrossRef](#)]
29. Weng, T.-F.; Ho, M.-S.; Sivakumar, C.; Balraj, B.; Chung, P.-F. VLS growth of pure and Au decorated β-Ga₂O₃ nanowires for room temperature CO gas sensor and resistive memory applications. *Appl. Surf. Sci.* **2020**, *533*, 147476. [[CrossRef](#)]
30. Kim, J.-H.; Mirzaei, A.; Kim, H.W.; Kim, S.S. Realization of Au-decorated WS₂ nanosheets as low power-consumption and selective gas sensors. *Sens. Actuators B* **2019**, *296*, 126659. [[CrossRef](#)]
31. Park, H.; Kim, J.-H.; Vivod, D.; Kim, S.; Mirzaei, A.; Zahn, D.; Park, C.; Kim, S.S.; Halik, M. Chemical-recognition-driven selectivity of SnO₂-nanowire-based gas sensors. *Nano Today* **2021**, *40*, 101265. [[CrossRef](#)]
32. Choi, S.-W.; Katoch, A.; Kim, J.-H.; Kim, S.S. Prominent reducing gas-sensing performances of n-SnO₂ nanowires by local creation of p-n heterojunctions by functionalization with p-Cr₂O₃ nanoparticles. *ACS Appl. Mater. Interfaces* **2014**, *6*, 17723–17729. [[CrossRef](#)] [[PubMed](#)]
33. Song, X.; Xu, Q.; Zhang, T.; Song, B.; Li, C.; Cao, B. Room-temperature, high selectivity and low-ppm-level triethylamine sensor assembled with Au decahedrons-decorated porous α-Fe₂O₃ nanorods directly grown on flat substrate. *Sens. Actuators B* **2018**, *268*, 170–181. [[CrossRef](#)]
34. Zhu, M.; Zhai, C.; Fujitsuka, M.; Majima, T. Noble metal-free near-infrared-driven photocatalyst for hydrogen production based on 2D hybrid of black Phosphorus/WS₂. *Appl. Catal. B* **2018**, *221*, 645–651. [[CrossRef](#)]
35. Kwak, C.-H.; Kim, T.-H.; Jeong, S.-Y.; Yoon, J.-W.; Kim, J.-S.; Lee, J.-H. Humidity-independent oxide semiconductor chemiresistors using terbium-doped SnO₂ yolk-shell spheres for real-time breath analysis. *ACS Appl. Mater. Interfaces* **2018**, *10*, 18886–18894. [[CrossRef](#)]
36. Choi, K.-I.; Kim, H.-J.; Kang, Y.C.; Lee, J.-H. Ultrasensitive and ultrasensitive detection of H₂S in highly humid atmosphere using CuO-loaded SnO₂ hollow spheres for real-time diagnosis of halitosis. *Sens. Actuators B* **2014**, *194*, 371–376. [[CrossRef](#)]
37. Gao, Z.; Song, G.; Zhang, X.; Li, Q.; Yang, S.; Wang, T.; Li, Y.; Zhang, L.; Fu, Y. A facile PDMS coating approach to room-temperature gas sensors with high humidity resistance and long-term stability. *Sens. Actuators B* **2020**, *325*, 128810. [[CrossRef](#)]
38. Lim, T.; Kang, Y.; Jeong, S.-M.; Ju, S. Thermally nonreactive and chemically reactive metal-oxide-nanowire transistor covered with aerogel-microsphere-thin-film-based selective filter. *Mater. Res. Express* **2018**, *5*, 116402. [[CrossRef](#)]
39. Mirzaei, A.; Kim, J.-H.; Kim, H.W.; Kim, S.S. Resistive-based gas sensors for detection of benzene, toluene and xylene (BTX) gases: A review. *J. Mater. Chem. C* **2018**, *6*, 4342–4370. [[CrossRef](#)]
40. Mirzaei, A.; Lee, J.-H.; Majhi, S.M.; Weber, M.; Bechelany, M.; Kim, H.W.; Kim, S.S. Resistive gas sensors based on metal-oxide nanowires. *J. Appl. Phys.* **2019**, *126*, 241102. [[CrossRef](#)]
41. Kim, H.-J.; Lee, J.-H. Highly sensitive and selective gas sensors using p-type oxide semiconductors: Overview. *Sens. Actuators B* **2014**, *192*, 607–627. [[CrossRef](#)]

42. Chen, Z.; Wang, J.; Cao, N.; Wang, Y.; Li, H.; de Rooij, N.F.; Umar, A.; Feng, Y.; French, P.J.; Zhou, G. Three-dimensional graphene-based foams with “greater electron transferring areas” deriving high gas sensitivity. *ACS Appl. Nano Mater.* **2021**, *4*, 13234–13245. [[CrossRef](#)]
43. Chen, Z.; Wang, J.; Wang, Y. Strategies for the performance enhancement of graphene-based gas sensors: A review. *Talanta* **2021**, *235*, 122745. [[CrossRef](#)] [[PubMed](#)]
44. Kim, J.W.; Kim, A. Absolute work function measurement by using photoelectron spectroscopy. *Curr. Appl. Phys.* **2021**, *31*, 52–59. [[CrossRef](#)]
45. Michaelson, H.B. The work function of the elements and its periodicity. *J. Appl. Phys.* **1977**, *48*, 4729. [[CrossRef](#)]
46. Hübner, M.; Koziej, D.; Grunwaldt, J.-D.; Weimar, U.; Barsan, N. Au clusters related spill-over sensitization mechanism in SnO₂-based gas sensors identified by operando HERFD-XAS, work function changes, DC resistance and catalytic conversion studies. *Phys. Chem. Chem. Phys.* **2012**, *14*, 13249–13254. [[CrossRef](#)]
47. Panda, D.; Nandi, A.; Datta, S.K.; Saha, H.; Majumdar, S. Selective detection of carbon monoxide (CO) gas by reduced graphene oxide (rGO) at room temperature. *RSC Adv.* **2016**, *6*, 47337–47348. [[CrossRef](#)]
48. Quyang, C.; Chen, Y.; Qin, Z.; Zeng, D.; Zhang, J.; Wang, H.; Xie, C. Two-dimensional WS₂-based nanosheets modified by Pt quantum dots for enhanced room-temperature NH₃ sensing properties. *Appl. Surf. Sci.* **2018**, *455*, 45–52.
49. Aykanat, A.; Meng, Z.; Stolz, R.M.; Morrell, C.T.; Mirica, K.A. Bimetallic two-dimensional metal-organic frameworks for the chemiresistive detection of carbon monoxide. *Angew. Chem.* **2022**, *134*, e202113665. [[CrossRef](#)]
50. Absalan, S.; Nasresfahani, S.; Schikhi, M.H. High-performance carbon monoxide gas sensor based on palladium/tin oxide/porous graphitic carbon nitride nanocomposite. *J. Alloys Compd.* **2019**, *795*, 79–90. [[CrossRef](#)]
51. Molavi, R.; Sheikhi, M.H. Facile wet chemical synthesis of Al doped CuO nanoleaves for carbon monoxide gas sensor applications. *Mater. Sci. Semicond. Process.* **2020**, *106*, 104767. [[CrossRef](#)]